2014

Accordion Effect in Plasma Channels: Generation of Tunable Comb-Like Electron Beams

Serguei Y. Kalmykov
University of Nebraska-Lincoln, s.kalmykov.2013@ieee.org

Bradley Allan Shadwick
University of Nebraska-Lincoln, shadwick@unl.edu

I. Ghebregziabher
1845 F Street Lincoln, NE

X. Davoine
CEA, DAM, DIF Arpajon F-91297 France

R. Lehe
Laboratoire d'Optique Appliqu´ee ENSTA-CNRS-´ Ecole Polytechnique UMR 7639, 91761 Palaiseau France

See next page for additional authors

Plasma Sciences (ICOPS) held with 2014 IEEE International Conference on High-Power Particle Beams (BEAMS), 2014 IEEE 41st International Conference on
Pages: 1 - 6, DOI: 10.1109/PLASMA.2014.7012740

Accordion Effect in Plasma Channels: Generation of Tunable Comb-Like Electron Beams

S. Y. Kalmykov, B. A. Shadwick
Department of Physics & Astronomy
University of Nebraska-Lincoln
Lincoln, NE 68588-0299, USA
Email: skalmykov2@unl.edu

I. Ghebregziabher
1845 F Street
Lincoln, NE 68508
USA

X. Davoine
CEA, DAM, DIF
Arpajon F-91297
France

R. Lehe, A. F. Lifschitz, V. Malka
Laboratoire d'Optique Appliquée
ENSTA-CNRS-École Polytechnique
UMR 7639, 91761 Palaiseau
France

***Abstract*—Propagating a short, relativistically intense laser pulse in a plasma channel makes it possible to generate comb-like electron beams for advanced radiation sources. The ponderomotive force of the leading edge of the pulse expels all electrons facing the pulse. The bare ions attract the ambient plasma electrons, forming a closed bubble of electron density confining the pulse tail. The cavity of electron density evolves slowly, in lock-step with the optical driver, and readily traps background electrons. The combination of a bubble (a self-consistently maintained, "soft" hollow channel) and a preformed channel forces transverse flapping of the laser pulse tail, causing oscillations in the bubble size. The resulting periodic injection produces a sequence of background-free, quasi-monoenergetic bunches of femtosecond duration. The number of these spectral components, their charge, energy, and energy separation is sensitive to the channel radius and pulse length. Accumulation of noise (continuously injected charge) can be prevented using a negatively chirped drive pulse with a bandwidth close to a one-half of the carrier wavelength. As a result of dispersion compensation, self-steepening of the pulse is reduced, and continuous injection almost completely suppressed. This level of control on a femtosecond time scale is hard to achieve with conventional accelerator techniques. These comb-like beams can drive high-brightness, tunable, multi-color γ-ray sources.**

I. Introduction

Laser-plasma accelerators (LPAs), driven by compact short-pulse, multi-terawatt lasers, have become a popular scientific instrument [1]. Their ability to deliver GeV-scale, background-free, fs-duration electron beams [2], [3], with a beam quality competitive with standard linear accelerators [4], is an asset for the design of all-optical γ-ray sources, featuring the unprecedented degree of control over the radiation spectrum [5]. This flexibility is rooted in the nature of the driver – a relativistically intense laser pulse. The radiation pressure of the pulse creates complete electron cavitation in an underdense plasma, leaving the background ions unperturbed [6]–[8]. The resulting "bubble" of electron density guides the pulse over many Rayleigh lengths while maintaining GV/cm-scale accelerating and focusing gradients [9]. The shape of the bubble evolves slowly, in lock-step with the optical driver, making it possible to trap initially quiescent background electrons, eliminating the need for an external photocathode [10]. The electron injection and acceleration process can thus be controlled by purely optical means [11]–[13], thereby adjusting the properties of electron beams to the demands of a given application.

Progress in applications demands the design of a miniature GeV-scale accelerator, driven by a high-repetition-rate, 10-TW-class laser. Reaching this energy over a few-mm distance requires an accelerating gradient as high as 10 GV/cm, which, in turn, dictates acceleration in the blowout regime in highly dispersive, dense plasmas ($\sim 10^{19}$ cm^{-3}). This choice presents a number of challenges. High-contrast, negative gradients of the nonlinear index co-propagate with the drive pulse, locally reducing its frequency by a large fraction of the carrier frequency [10], [11], [13]–[17]. The negative group velocity dispersion (GVD) of the plasma concurrently transforms the red-shifted pulse into a relativistic optical shock [18], [19], causing the bubble to constantly expand and trap background electrons, degrading electron beam quality [10]–[13], [20], [21]. To avoid this, we propose to compensate for the nonlinear reduction in frequency (exceeding $-\omega_0/2$) with a careful choice of the initial laser phase [22]. To be practically effective, this approach needs broad spectrum amplifiers delivering few-Joule, near-IR laser pulses with the bandwidth approaching one-half of the carrier wavelength {such as the future Petawatt Field Synthesizer (PFS) [23]}. By temporally advancing the high frequency components of the incident pulse (i.e. introducing a *negative frequency chirp*), we reduce the positive chirp produced by the plasma wake excitation. The negatively chirped pulse (NCP) thus remains uncompressed through electron dephasing, continuous injection remains suppressed, and the quasi-monoenergetic (QME) electron bunch remains dominant. As a bonus, the higher average frequency of the pulse, together with slower etching of its front, effectively increases the dephasing length, boosting electron energy [11]–[13]. This technique of dispersion compensation, combined with tailoring of the target, helps produce high-quality electron beams in formats other than a single QME bunch. Propagating

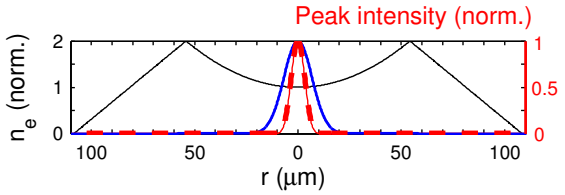

Fig. 1. Radial profile of electron density (left axis) and normalized intensity of the NCP in a cross-section taken at the peak intensity (right axis). (WAKE simulation.) Density on axis $n_0 = 6.5 \times 10^{18}$ cm^{-3}. Blue curve: initial distribution of intensity ($z = 0$, matched spot). Red curves: distributions of intensity at $z = 2$ mm (thin solid line) and 2.5 mm (thick dashed line). The most intense segment of the pulse self-guides with almost invariable spot size, roughly one-half of the channel-matched spot size.

978-1-4799-2713-5/14/$31.00 ©2014 IEEE

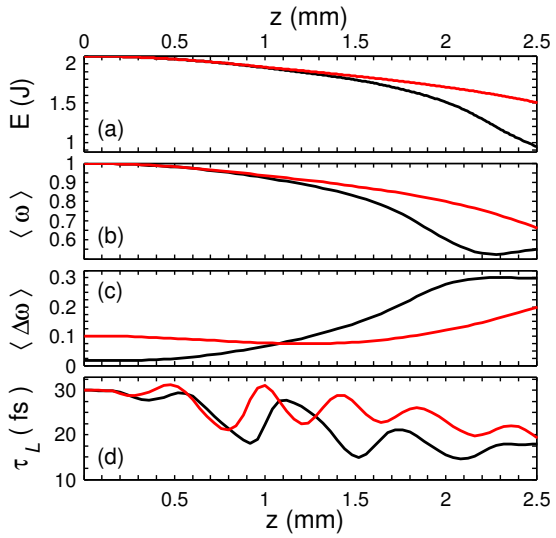

Fig. 2. Evolution of (a) laser pulse energy; (b) mean frequency (in units of ω_0); (c) RMS bandwidth (in units of ω_0); (d) pulse length computed from the ζ-variance of the energy density on axis. (WAKE simulations.) Black – the reference case; red – the NCP in a channel. The pulse propagates towards positive z. The chirp and channel together reduce depletion, frequency red-shift, spectral broadening, and contraction of the pulse (cf. also Fig. 3).

the NCP in a channel [24] suppresses diffraction of its leading edge, further reducing self-steepening. More importantly, the channel forces periodic oscillations of the bubble size, bringing about periodic self-injection [25]. The resulting polychromatic ("comb-like") electron beams consist of several high-quality, multi-100 MeV QME components each carrying 100 pC-scale charge. The number of these components can be controlled by varying the channel radius, whereas their mean energy and energy separation is controlled by changing the plasma length [12], [26]. Negative chirp minimizes the continuous energy background, improving spectral separation and energy spread of individual components. Such clean multi-color beams, unavailable with standard accelerator technology, may find a unique application as drivers for table-top short-pulse optical sources from near-IR to γ-ray range [5], [27].

II. Simulation Framework

Physical processes underlying the all-optical manipulations of the LPA are explored using reduced and full particle-in-cell simulations. Fast quasistatic simulations using the fully relativistic, cylindrically symmetric, time-averaged (over $1/\omega_0$), extended paraxial code WAKE [6], [14] shed light on the physical nature of the continuous injection [11] and help retrieve the laser pulse phase profile sufficient to disrupt formation of the relativistic optical shock. Accurate self-consistent simulations of electron phase space dynamics are carried out with the fully explicit, quasi-cylindrical code CALDER-Circ [28], which uses a numerical Cherenkov-free electromagnetic solver [29] and third-order splines for macroparticles. These features, in combination with the fine grid ($\Delta z = \Delta r/16 = 0.125c/\omega_0 = 16$ nm, where $r^2 = x^2 + y^2$) and large number of particles per cell (20) maintain low sampling noise, negligibly low numerical dispersion, and also avoids numerical emittance dilution.

The interaction regime corresponds to that considered in [11], [12]. The plasma spans from $z = 0$ to 3 mm, having 0.5 mm-length linear entrance and exit ramps, and a 2 mm longitudinally flat section with the density $n_0 = 6.5 \times 10^{18}$ cm^{-3}. The linearly polarized, 70 TW pulse with the carrier wavelength $\lambda_0 = 0.805$ μm propagates toward positive z. The normalized vector potential in the focal plane is Gaussian, $a(z=0) = a_0 \exp[-(r/r_0)^2 - 2\ln 2 (t/\tau_L)^2 + i\varphi(t)]$, with $a_0 = 3.27$, $\tau_L = 30$ fs, $r_0 = 13.6$ μm. The rate of the phase variation defines the instantaneous frequency, $\omega(t) = -d\varphi/dt = \omega_0 - (4\ln 2)(\kappa/\tau_L)^2 t$, where $\omega_0 = 2\pi c/\lambda_0$. Simulations with a 30 fs-length, transform-limited pulse, or TLP ($\kappa = 0$), are referred to as *the reference case*. To combat self-steepening, we increase the bandwidth by a factor of 6 ($\kappa = 2.4323$), thus temporally advancing high frequencies; the NCP in this format may be obtained by under-compressing a 420-TW, 5-fs pulse of the PFS [23]. A detailed comparative study of the TLP and NCP evolution in a *uniform* plasma was presented in [11]. We complement this study by placing the pulse in a leaky channel matched to the spot size of the incident pulse [24] (cf. Fig. 1):

$$n_e(r) = \begin{cases} n_0(1 + r^2/r_{\rm ch}^2), & \text{for } r \le r_{\rm ch} \\ 2n_0(2 - r/r_{\rm ch}), & \text{for } r_{\rm ch} < r \le 2r_{\rm ch} \\ 0, & \text{for } r > 2r_{\rm ch}. \end{cases}$$

The channel further mitigates the pulse self-steepening and yields, as a bonus, new features in the electron beam.

III. Results and Discussion

A. Preventing Formation of Relativistic Optical Shock

The large bandwidth and negative chirp significantly reduce energy depletion, average frequency red-shift, and self-compression of the drive pulse. Figures 2(b) and 2(c) show radially integrated mean frequency and frequency variance [16]

$$\langle \omega(z) \rangle = A^{-1} \int_0^\infty r\,{\rm d}r \int_0^\infty \omega |a(r,z,\omega)|^2\,{\rm d}\omega,$$
$$\langle \Delta\omega(z) \rangle^2 = A^{-1} \int_0^\infty r\,{\rm d}r \int_0^\infty (\omega - \langle\omega\rangle)^2 |a(r,z,\omega)|^2\,{\rm d}\omega,$$

where $a(r,z,\omega) = \int_{-\infty}^{+\infty} a(r,z,\zeta) {\rm e}^{-i(\omega_0-\omega)\zeta}\,{\rm d}\zeta$ is the Fourier transform with respect to $\zeta = z/c - t$, and $A = \int_0^\infty r\,{\rm d}r \int_0^\infty |a(r,z,\omega)|^2\,{\rm d}\omega$. Figure 2(d) shows the pulse length computed as a ζ-variance of the energy density on axis,

$$\tau_L(z) = \left(8\ln 2 B^{-1} \int_{-\infty}^{\infty} (\zeta - \langle\tau\rangle)^2 |a(0,z,\zeta)|^2\,{\rm d}\zeta \right)^{1/2},$$

where $\langle\tau\rangle = B^{-1} \int_{-\infty}^{\infty} \zeta\, |a(0,z,\zeta)|^2\,{\rm d}\zeta$ is the position of the pulse centroid, and $B = \int_{-\infty}^{\infty} |a(0,z,\zeta)|^2\,{\rm d}\zeta$. Figures 2(a) and 2(b) indicate that in the reference case the pulse energy and mean frequency drop by 50% by the end of the interaction, with a nearly 10-fold increase in the frequency variance [Fig. 2(c)]. Conversely, an NCP propagating in the channel experiences merely 30% reduction in energy and mean frequency, with the initial bandwidth preserved through $z \approx 2$ mm (or 80% of the interaction length). As a result, pulse compression is noticeably reduced [cf. Fig. 2(d)].[1]

Figure 3 complements the integral characteristics displayed in Fig. 2 and links longitudinal distortion of the pulse [panels

[1] Oscillations in $\tau_L(z)$ result from periodic focusing of the pulse tail inside a bubble (cf. Fig. 4). For a pulse of duration much shorter than the bubble length such oscillations are absent [13].

(a), (b)] to the local frequency shift on axis [(c), (d)]. The shift is extracted from the complex envelope of the vector potential, $a(0,z,\zeta)=|a|\exp(i\phi)$, using two independent methods [14]. First, the Wigner transform of the envelope, $\mathcal{W}(\zeta,\omega)=\int_{-\infty}^{+\infty} a\left(\zeta+\frac{\zeta'}{2},z\right)a^*\left(\zeta-\frac{\zeta'}{2},z\right)\mathrm{e}^{-i(\omega_0-\omega)\zeta}\,\mathrm{d}\zeta'$, yields the distribution of "photon density" in the "photon phase space." Secondly, the "instantaneous" frequency is calculated as the rate of the envelope phase change, $\omega(\zeta)=\omega_0-\mathrm{d}\phi/\mathrm{d}t=\omega_0+\partial\phi/\partial\zeta$. The pulse leading edge rides on the co-moving negative gradient in the nonlinear index. The positive frequency chirp develops along the gradient, red-shifting the pulse head by a large fraction of the carrier frequency. Radially integrated spectral power $S(z,\omega)=\int_0^\infty \omega^2|a(r,z,\omega)|^2 r\,\mathrm{d}r$ shown in Fig. 3(e) demonstrates an order-of-magnitude increase of the pulse bandwidth in the reference case, in agreement with Fig. 2(c).

In the reference case, negative GVD slows down the red-shifted frequency components, compressing the pulse to a nearly single-cycle optical shock of highly relativistic intensity ($|a|\approx 16$) [cf. Figs. 3(a) and 3(c)]. The shock acts on the ambient plasma electrons as a snow-plow, causing elongation of the bubble and continuous injection [11]. The mid-IR photons further slide into the bubble, mixing with the unshifted radiation, red-shifting the entire pulse by the end of the interaction. Mixing radiation of different frequencies and uncorrelated phases leads to sharp variations of the envelope phase, making the local frequency poorly defined, causing oscillations of the envelope in the tail area.

Chirp and channel together delay formation of the optical shock. The channel suppresses diffraction of the leading edge, reducing its steepening [12]. Temporal advancement of high frequencies partly compensates for the nonlinear red-shift, preserving the pulse bandwidth for a long time. The red-shift remains localized at the leading edge [cf. Fig. 3(d)]. There is no sign of photon phase mixing. The instantaneous frequency thus remains well-defined and single-valued, showing minimal oscillations. The pulse in Fig. 3(b) is not yet fully compressed, and the intensity build-up is only about a half of that of the reference case. Weaker compression of the NCP reduces the snow-plow effect thereby suppressing the bubble expansion.

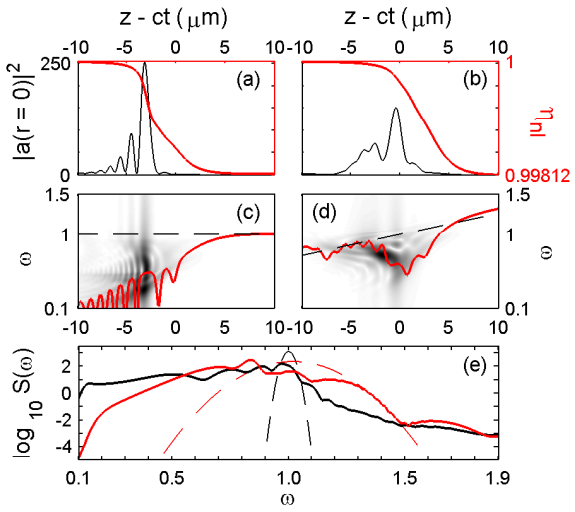

Fig. 3. Preventing pulse self-steepening with negative frequency chirp (WAKE simulations.) Panels (a) and (c) correspond to the reference case, and (b) and (d) to the case of an NCP propagating in a channel. The pulse propagates from left to right. All quantities correspond to $z = 2.2$ mm (the dephasing limit in the reference case). All quantities in panels (a)–(d) are shown on axis: (a), (b) lineouts of the normalized intensity, $|a|^2$ (left axes, black curves), and nonlinear refractive index (right axes, red curves); and (c), (d) absolute value of the Wigner transform (grayscale) and instantaneous frequency extracted from the envelope phase. Panel (e) shows radially integrated spectral power in the reference case (black) and in the case of NCP propagating in a channel (red); frequency is in units of ω_0. Dashed curves in panels (c)-(e) correspond to the incident pulse. The co-moving negative slope of the index red-shifts the frequency at the pulse leading edge. In the reference case, mid-IR photons, delayed by the negative GVD of the plasma, build up a relativistic optical shock and further slide into the bubble, mixing with unshifted radiation. The negative chirp reduces frequency red-shift and localizes it to the pulse leading edge, thus reducing self-steepening.

B. Accordion Effect and Periodic Injection

Propagation in the channel adds new features to the pulse evolution, leading to generation of electron beams in unconventional formats. Figure 4 examines *transverse* evolution of the NCP in the uniform plasma and in the channel, linking it to the process of electron self-injection. In the uniform plasma, the accelerating phase (the region inside the bubble where the longitudinal electric field is negative) oscillates only once [between points marked (CF1) and (CF3) in Fig. 4(a)], giving way to continuous expansion afterwards. A single QME bunch with a weak tail is thus created [11]. Conversely, the bubble propagating in a channel oscillates at least twice between points marked (CC1) and (CC5), producing two distinct features in collection volume [initial longitudinal and radial positions of high-energy electrons at dephasing shown in Fig. 4(b)]. Collection phase space and energy spectrum in Figs. 5(c) and 5(d) indicate that these features correspond to narrow-bandwidth QME bunches well separated in energy.

Oscillation of the accelerating phase (*the accordion effect*) was found to be the cause of periodic self-injection and creation of multiple QME beams in a uniform plasma [30]. Generation of comb-like beams in channels was observed as well [25], [26]. In both situations (and in the regime considered here) the laser pulse and the bubble are comparable in length. The pulse can be thus split into two segments – the most intense one ("the head"), located in the region of the index gradient at the leading edge, and less intense tail confined within the bubble. Figures 4(c) and 4(CC1)–4(CF6) demonstrate that the head is quite insensitive to transverse non-uniformity of the ambient plasma. It self-guides with a steadily varying spot, showing no oscillations. Furthermore, suppressing diffraction of the leading edge with the preformed channel almost freezes the head spot size (this can also be seen in Fig. 1). As a result, the collection radius (initial radial offset of self-injected electrons, close to the local spot size of head) shown in Fig. 4(b) remains uniform throughout acceleration. Thus, contrary to the earlier conjectures [25], [26], the channel *stabilizes* the most intense segment of the pulse, preventing undamped "betatron oscillations."

The pulse tail, on the other hand, is naturally unmatched to the self-consistently maintained soft hollow channel – the bubble. Snapshots of the pulse intensity taken at the points of full expansion/contraction of the bubble [Figs. 4(CC1)–4(CF6)] show that the tail flaps, driving the bubble boundaries sidewards, changing the bubble size. In a uniform plasma, the

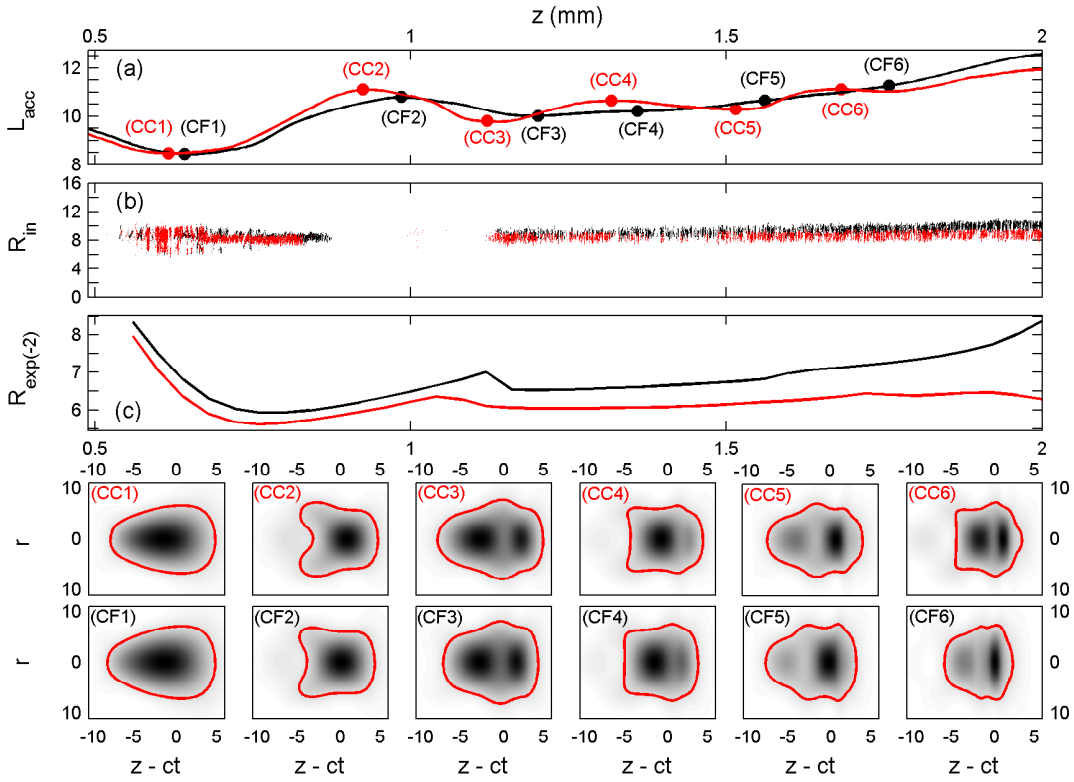

Fig. 4. Accordion effect in a plasma channel. The NCP propagates in a longitudinally uniform channel [red in panels (a)–(c)] and in a flat plasma [black in (a)–(c)]. All lengths are in microns, unless specified differently. CALDER-Circ simulations yield the length of the accelerating phase on axis (roughly, half-length of the bubble), (a), and collection volume of electrons crossing the plane $z = 2.2$ mm, (b). Initial radial offsets of injected electrons in panel (b) correspond to a cylindrical shell with a local radius close to the radius of the laser pulse head. WAKE simulations yield the evolution of the laser beam radius in the highest-intensity cross-section (at e^{-2} of the peak intensity) [panel (c)] and pulse intensity snapshots (CC1)–(CF6) at the points of full expansion and contraction of the bubble, labeled accordingly in panel (a). The pulse propagates to the right, tags "CC" and "CF" stand for "chirp-channel" and "chirp-flat". The grayscale shows distributions of intensity normalized to the local peak intensity, encircled by the intensity iso-contours at e^{-2} of the peak. Oscillations of the bubble size [panel (a)] are uncorrelated with the evolution of the most intense segment of the pulse [panel (c)]. The pulse head propagates with almost invariable spot, whereas the tail flaps inside the bubble, driving the bubble walls sidewards, causing bubble expansion and electron self-injection. In the uniform plasma, flapping subsides after the point (CF3), giving way to steady bubble expansion and weak continuous injection. In the channel, flapping persists, yielding two oscillations of the bubble size and two distinct consecutive injections producing two high-energy QME beams [cf. Fig. 5(d)].

flapping subsides. The addition of the low-contrast external channel supports the flapping, leading to at least 2.5 periods of bubble oscillations between the points marked (CC1) and (CC5) in Fig. 4(a). We find that reducing the channel radius, matching the channel to the *self-guided* rather than incident pulse spot size, destabilizes the tail even further, yielding another period of bubble oscillation, adding a third QME electron bunch accelerated in the first bucket (these details will be presented in a separate publication).

Reducing the amount of radiation confined inside the bubble effectively eliminates the accordion effect [13]. Figure 6 shows that clipping the pulse tail (i.e. reducing the pulse length from 30 to 20 fs while keeping the same 70 TW power and the same frequency bandwidth) leads to a single oscillation of the bubble size, followed by a steady slow expansion. This yields a single high-charge QME bunch with a weak tail, similarly to the uniform-plasma case [11]. Changing the channel radius and/or the NCP length (as permitted by the bandwidth) thus effectively controls the output of the acceleration process and the electron beam structure (from comb-like to quasi-monoenergetic), while keeping a low level of background.

Last but not least, the data presented in Figs. 4–6 show that, in all instances, whether self-injection is continuous or periodic, into the first or the second bucket, in a uniform plasma or in a channel, *all* electrons accelerated through dephasing are collected from the cylindrical shell, as predicted by theory [10], [11], [30]. There is no evidence of longitudinal injection reported earlier for a similar regime [31]. Stable propagation of the pulse head, showing no signs of "betatron oscillations," as well as the collection volume inconsistent with longitudinal wavebreaking, rules out both "parametric resonance" and periodic longitudinal wavebreaking [25], [26] as physical mechanisms responsible for the generation of these tunable comb-like electron beams.

C. Properties of Electron Beams

The dynamics of electron injection in the channel is discussed in detail in [12]. QME beams statistics for the cases displayed in Figs. 5 and 6 are summarized in Table I. Table I shows: total charge, Q; mean energy, $\langle E\rangle$; dispersion of energy, σ_E; root-mean-square (RMS) normalized transverse emittance, $\varepsilon_\perp^N = 2^{-1/2}[(\varepsilon_x^N)^2+(\varepsilon_y^N)^2]^{1/2}$, where $\varepsilon_i^N = (m_e c)^{-1}[(\langle p_i^2\rangle - \langle p_i\rangle^2)(\langle r_i^2\rangle - \langle r_i\rangle^2) - (\langle p_i r_i\rangle - \langle r_i\rangle\langle p_i\rangle)^2]^{1/2}$; RMS divergence

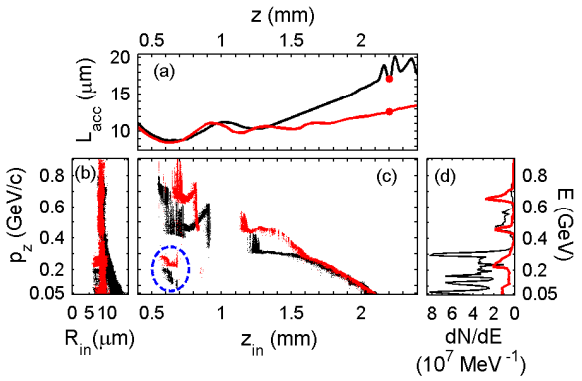

Fig. 5. Dynamics of electron injection in the reference case (black) and in the case of NCP propagating in a channel (red) (CALDER-Circ simulations). (a) Length of the accelerating phase on axis vs. propagation length. (b), (c) Transverse (longitudinal) collection phase space [initial radial (longitudinal) positions vs. final longitudinal momenta] of electrons crossing the plane $z = 2.2$ mm [red marker in panel (a)]. The channel suppresses diffraction of the pulse leading edge, keeping the collection radius [red markers in panel (b)] constant. In a channel, the bubble size oscillates twice between $z = 0.8$ and 1.55 mm, producing two distinct groups of QME electrons in panel (c). The group encircled by a blue ellipse is accelerated into the second bucket. (d) Electron energy spectra. The negative chirp and the channel suppress continuous injection so effectively as to make electrons from the second bucket ($E \approx 250$ MeV) stand clearly against the weak low-energy background.

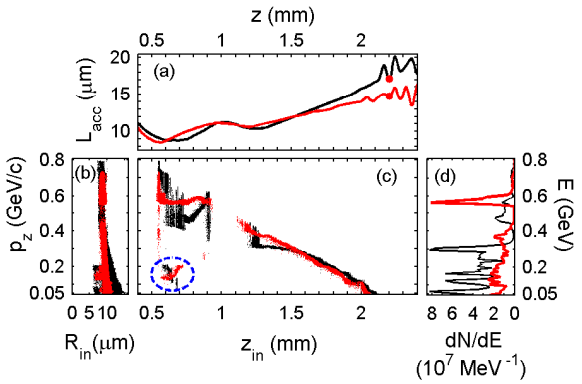

Fig. 6. Same as Fig. 5 except the NCP length is 20 fs (rather than 30 fs), with 70 TW power and frequency bandwidth equivalent to a 5 fs transform-limited duration. Clipping the pulse tail suppresses the bubble oscillations, yielding a single QME bunch with an average flux 3.5 times higher than in the reference case, and a weak tail. As in Figs. 4 and 5, all injected electrons have radial offsets close to the laser pulse spot size; there is no evidence of longitudinal injection from the near-axis region.

$\sigma_\alpha = 2^{-1/2}[\sigma_{\alpha x}^2 + \sigma_{\alpha y}^2]^{1/2}$, where $\sigma_{\alpha i} = \langle p_z \rangle^{-1}(\langle p_i^2 \rangle - \langle p_i \rangle^2)^{1/2}$; and the average flux $\langle F \rangle = Q/\sigma_E$. Statistics of the continuous background are collected in Table II.

The energy spectra in the reference case [black curves in Figs. 5(d) and 6(d)] are fully dominated by the high-charge energy tail, which contains 85% the total charge accelerated above 50 MeV. The chirp and the channel bring the tail down, reducing the charge by a factor 2–4, and the average flux by a factor 2.75–4.25 (depending on the pulse length), while roughly preserving the net charge of the QME components.[2] The chirp and the channel also reduce the energy spread of the QME components against the reference case. The highest energy component of the tri-color beam [Fig. 5(d)] receives 30% energy boost against the reference case, while acceleration in the second bucket adds the third component to the energy comb. The QME bunch accelerated through dephasing in the reference case absorbs 8%, and the tail about 15% of the incident pulse energy. Carrying out acceleration with a 20 fs NCP over the same distance in the channel changes these numbers to 16.5% and 10%, respectively. Increasing the NCP duration to 30 fs changes the energy balance, with 10.5% going to the comb-like beam, and only 3% to the tail.

The energy and energy separation of the QME bunches can be controlled by changing the acceleration length. Owing to the stabilizing effect of the chirp, the acceleration distance can be varied safely, without accumulation of the background [12]. The residual background is not a deal-breaker for inverse Compton scattering (ICS) sources. Preliminary simulations of the ICS of a narrow-bandwidth laser beam ($\lambda = 0.8$ μm, $\Delta\lambda/\lambda = 0.02$) from the tri-color electron beam of Fig. 5 show that the comb-like structure imprints onto the scattered radiation spectrum, yielding a tunable tri-color γ-ray flashes with the peak flux in the range 10^8 ph MeV^{-1} sr^{-1}, and the energy of QME components (energy spread 20–40%) ranging from 1 to 12 MeV. Inclusion of the low-energy background affects only the lowest-energy component, actually increasing its flux. QME beam of Fig. 6 yields the γ-ray signal centered at 7 MeV, with roughly a 30% energy spread and the peak flux 2.5×10^8 ph MeV^{-1} sr^{-1}.

[2]Importantly, the channel alone is unable to suppress the tail [12].

IV. Summary and Outlook

The numerical simulations presented here demonstrate production of GeV-scale, clean comb-like electron beams of fs-scale duration (a beam format inaccessible with standard acceleration techniques) in a miniature, mm-size LPA. Propagating the drive pulse in the plasma channel destabilizes the pulse tail confined within the soft accelerating bucket – the electron density bubble. Transverse flapping of the unmatched tail causes oscillations in the bubble size in the course of propagation. This accordion effect results in the periodic injection and subsequent acceleration of comb-like electron beams. Using a drive pulse with a broad frequency spectrum (equivalent to the sub-2-cycle transform-limited duration) and introducing a negative chirp prevents pulse self-compression into the relativistic optical shock, thereby suppressing continuous injection and accumulation of low-energy background in electron spectra. The channel radius and the pulse length are important parameters, controlling the number of spectral components in the beam, whereas their energy and energy difference can be controlled by changing the plasma length. Low energy spread and clear separation of GeV-scale spectral components in energy, as well as a minimal amount of noise (resulting from all-optical control of self-injection), make our comb-like beams attractive for advanced radiation sources. They can drive compact, all-optical, multi-color ICS γ-ray sources [5]. Alternatively, by separating the QME components in a magnetic electron spectrometer and using beam delay lines, or selectively focusing them with highly chromatic magnetic quadrupole lenses [32], one can use our multi-color beams as drivers of compact, tunable, synchronized, pulsed broad-bandwidth radiation sources [27].

TABLE I. STATISTICS OF THE QME BEAMS [FIGS. 5(D) AND 6(D)]

	Beam 1 [a]	Beam 1 [b]	Beam 1 [c]	Beam 2 [c]	Beam 3 [c,d]
Q (pC)	330	400	200	117	85.5
$\langle E \rangle$ (MeV)	540	585	700	503	245
σ_E (MeV)	88	32	36	36	18.5
$\varepsilon_\perp^N$ (mm mrad)	0.57	0.85	1.0	0.75	2.08
σ_α (mrad)	2.00	2.60	2.1	2.50	6.60
$\langle F \rangle$ [e]	3.75	12.5	5.5	3.25	4.60

[a] reference case [Fig. 5(d), black]
[b] 20 fs NCP in the channel [Fig. 6(d), red]
[c] 30 fs NCP in the channel [Fig. 5(d), red]
[d] electrons from the second bucket only
[e] in pC MeV^{-1}.

TABLE II. STATISTICS OF THE BACKGROUND [FIGS. 5(D) AND 6(D)]

	Q (pC) [a]	$E_{\max}$ (MeV)	σ_α (mrad)	$\langle F \rangle$ (pC MeV^{-1}) [b]
Reference	1520	350	10.5	5.07
NCP, 30 fs [c]	360	350	5.50	1.20
NCP, 20 fs	735	450	8.50	1.84

[a] charge in the energy range $50\ \mathrm{MeV} < E < E_{\max}$
[b] average flux, $\langle F \rangle = Q/\Delta E$, $\Delta E = E_{\max} - 50$ MeV
[c] electrons from the first bucket only.

ACKNOWLEDGMENTS

The work of SYK and BAS is supported by the U.S. DOE Grant DE-SC0008382 and NSF Grant PHY-1104683. The CALDER-Circ simulations were performed using HPC resources of GENCI-CCRT and GENCI-CINES (grant 2013-057027). Inverse Compton scattering simulations were completed utilizing the Holland Computing Center of the University of Nebraska.

REFERENCES

[1] E. Esarey, C. B. Schroeder, and W. P. Leemans, "Physics of laser-driven plasma-based electron accelerators," *Rev. Mod. Phys.*, vol. 81, no. 3, pp. 1229-1285, Jul. 2009.

[2] S. Banerjee, N. D. Powers, V. Ramanathan *et al.*, "Generation of tunable, 100-800 MeV quasi-monoenergetic electron beams from a laser-wakefield accelerator in the blowout regime," *Phys. Plasmas*, vol. 19, no. 5, 056703, May 2012.

[3] S. Banerjee, S. Y. Kalmykov, N. D. Powers *et al.*, "Stable, tunable, quasimonoenergetic electron beams produced in a laser wakefield near the threshold for self-injection," *Phys. Rev. ST Accel. Beams*, vol. 16, no. 3, 031302, Mar. 2013.

[4] J. Park, Ch. Kim, J. Lee *et al.*, "Generation, transport, and detection of linear accelerator based femtosecond-terahertz pulses," *Rev. Sci. Instrum.*, vol. 82, no. 1, 013305, Jan. 2011.

[5] N. D. Powers, I. Ghebregziabher, G. Golovin *et al.*, "Quasi-monoenergetic and tunable X-rays from a laser-driven Compton light source," *Nat. Photon.*, vol. 8, pp. 28-31, Jan. 2014.

[6] P. Mora and T. M. Antonsen, Jr., "Electron cavitation and acceleration in the wake of an ultraintense, self-focused laser pulse," *Phys. Rev. E*, vol. 53, no. 3, pp. R2068-R2071, Mar. 1996.

[7] A. Pukhov and J. Meyer-ter-Vehn, "Laser wake field acceleration: the highly non-linear broken-wave regime," *Appl. Phys. B: Lasers Opt.*, vol. 74, no. 4-5, pp. 355-361, Apr. 2002.

[8] S. Y. Kalmykov, B. A. Shadwick, A. Beck, and E. Lefebvre, "Physics of quasi-monoenergetic laser-plasma acceleration of electrons in the blowout regime," in *Femtosecond-Scale Optics*, A. V. Andreev, Ed. Rijeka, Croatia: InTech, 2011, pp. 113-138.

[9] W. Lu, M. Tzoufras, C. Joshi *et al.*, "Generating multi-GeV electron bunches using single stage laser wakefield accelerationin a 3D nonlinear regime," *Phys. Rev. ST Accel. Beams*, vol. 10, no. 6, 061301, June 2007.

[10] S. Y. Kalmykov, A. Beck, S. A. Yi *et al.*, "Electron self-injection into an evolving plasma bubble: Quasi-monoenergetic laser-plasma acceleration in the blowout regime," *Phys. Plasmas*, vol. 18, 056704, May 2011.

[11] S. Y. Kalmykov, A. Beck, X. Davoine *et al.*, "Laser plasma acceleration with a negatively chirped pulse: all-optical control over dark current in the blowout regime," *New J. Phys.*, vol. 14, no. 3, 033025, Mar. 2012.

[12] S. Y. Kalmykov, B. A. Shadwick, and X. Davoine, "All-optical control of electron trapping in plasma channels," in *2013 19th IEEE Pulsed Power Conference (PPC)*, pp. 1–6; DOI: 10.1109/PPC.2013.6627518.

[13] S. Y. Kalmykov, X. Davoine, and B. A. Shadwick, "All-optical control of electron self-injection in millimeter-scale, tapered dense plasmas," *Nucl. Instrum. Methods in Phys. Res. A*, vol. 740, pp. 266-272, 2014.

[14] W. Zhu, J. P. Palastro, and T. M. Antonsen, Jr., "Studies of spectral modification and limitations of the modified paraxial equation in laser wakefield simulations," *Phys. Plasmas*, vol. 19, 033105, Mar. 2012.

[15] W. Zhu, J. P. Palastro, and T. M. Antonsen, Jr., "Pulsed mid-infrared radiation from spectral broadening in laser wakefield simulations," *Phys. Plasmas*, vol. 20, 073103, Jul. 2013.

[16] A. A. Balakin, A. G. Litvak, V. A. Mironov, and S. A. Skobelev, "Compression of femtosecond petawatt laser pulses in a plasma under the conditions of wake-wave excitation," *Phys. Rev. A*, vol. 88, no. 5, 023836, Feb. 2013.

[17] S. Shiraishi, C. Benedetti, A. J. Gonsalves *et al.*, "Laser red shifting based characterization of wakefield excitation in a laser-plasma accelerator," *Phys. Plasmas*, vol. 20, no. 6, 063103, June 2013.

[18] J. Faure, Y. Glinec, J. J. Santos *et al.*, "Observation of laser-pulse shortening in nonlinear plasma waves," *Phys. Rev. Lett.*, vol. 95, no. 20, 205003, Nov. 2005.

[19] A. Pipahl, E. A. Anashkina, M. Toncian *et al.*, "High-intensity few-cycle laser-pulse generation by the plasma-wakefield self-compression effect," *Phys. Rev. E*, vol. 87, no. 3, 033104, Mar. 2013.

[20] S. Kneip, S. R. Nagel, S. F. Martins *et al.*, "Near-GeV acceleration of electrons by a nonlinear plasma-wave driven by a self-guided laser pulse," *Phys. Rev. Lett.*, vol. 103, no. 3, 035002, July 2009.

[21] D. H. Froula, C. E. Clayton, T. Döppner *et al.*, "Measurements of the critical power for self-injection of electrons in a laser wakefield accelerator," *Phys. Rev. Lett.*, vol. 103, no. 21, 215006, Nov. 2009.

[22] G. P. Agarwal, *Nonlinear Fiber Optics*, 4th ed. San Diego, USA: Academic Press, 2006. Ch. 3.

[23] Zs. Major, S. Klingebiel, C. Skrobol *et al.*, "Status of the Petawatt Field Synthesizer – pump-seed synchronization measurements," *AIP Conf. Proc.*, vol. 1228, pp. 117-122, May 2010.

[24] H. M. Milchberg, T. R. Clark, C. G. Durfee III *et al.*, "Development and applications of a plasma waveguide for intense laser pulses," *Phys. Plasmas*, vol. 3, no. 5, pp. 2149-2155, May 1996.

[25] A. Oguchi, A. Zhidkov, K. Takano *et al.*, "Multiple self-injection in the acceleration of monoenergetic electrons by a laser wake field," *Phys. Plasmas*, vol. 15, no. 4, 043102, Apr. 2008.

[26] A. Zhidkov, J. Koga, T. Hosokai *et al.*, "Characterization of electron self-injection in laser wake field acceleration due to the parametric resonance," *Phys. Plasmas*, vol. 17, no. 8, 083101, Aug. 2010.

[27] C. Ronsivalle, M. P. Anania, A. Bacci *et al.*, "Large-bandwidth two-color free-electron laser driven by a comb-like electron beam," *New J. Phys.*, vol. 16, no. 3, 033018, Mar. 2014.

[28] A. F. Lifschitz, X. Davoine, E. Lefebvre *et al.*, "Particle-in-cell modelling of laser-plasma interaction using Fourier decomposition," *J. Comput. Phys.*, vol. 228, no. 5, pp. 1803-1814, Mar. 2009.

[29] R. Lehe, A. F. Lifschitz, C. Thaury, V. Malka, and X. Davoine, "Numerical growth of emittance in simulations of laser-wakefield acceleration," *Phys. Rev. ST Accel. Beams*, vol. 16, no. 2, 021301, Feb. 2013.

[30] S. Y. Kalmykov, S. A. Yi, A. Beck *et al.*, "Numerical modelling of a 10-cm-long multi-GeV laser wakefield accelerator driven by a self-guided petawatt pulse," *New J. Phys.*, vol. 12, no. 4, 045019, Apr. 2010.

[31] S. Corde, C. Thaury, A. F. Lifschitz *et al.*, "Observation of longitudinal and transverse self-injections in laser-plasma accelerators," *Nat. Commun.*, vol. 4, 1501, Feb. 2013.

[32] R. Weingartner, M. Fuchs, A. Popp *et al.*, "Imaging laser-wakefield-accelerated electrons using miniature magnetic quadrupole lenses," *Phys. Rev. ST Accel. Beams*, vol. 14, no. 5, 052801, May 2011.